Pixelated sintering of α-Al2O3

Iñaki Cornu, Maxime Cheype, Marion Baudier-Pons, Jean-François Léon, Samuel Couillaud, Fabrice Rossignol, Jean-Marc Heintz

Pixelated sintering of α-Al_2O_3

Iñaki Cornu [a,c,*], Maxime Cheype [a], Marion Baudier-Pons [c], Jean-François Léon [b], Samuel Couillaud [b], Fabrice Rossignol [a], Jean-Marc Heintz [c]

[a] IRCER, UMR CNRS 7315, University of Limoges, 12 rue Atlantis, F-87068 Limoges, France
[b] Galtenco Solutions Company, Parc Scientifique Unitec 1, F-33600 Pessac, France
[c] ICMCB, UMR CNRS 5026, Bordeaux INP, 87 Avenue du Docteur Schweitzer, F-33608 Pessac, France

ARTICLE INFO

Keywords:
Pixelated sintering
Spark plasma sintering
Pressure-less spark plasma sintering
Sintering path
α-Alumina

ABSTRACT

The sintering of α-alumina by a brand new and innovative technique, called pixelated sintering (PS), is here studied. Densification and grain growth by PS of perfectly controlled granular compacts are analysed and compared to results obtained using Spark Plasma Sintering (SPS) and Pressure-Less SPS (PL-SPS). Materials are exposed to the same temperature profiles whatever the sintering technique used in order to assess the potential of PS in terms of microstructure control. It is shown that PS can be used as an alternative technique to SPS for fast sintering with the advantages of a much simpler and cost-effective set-up, as well as a better control of the localised heat input. PS also appears to be a very modular technology in the way it controls the temperature gradients allowing its implementation for multi-step sintering approaches, as well as for the fabrication of large and complex parts.

1. Introduction

The permanent need to improve properties of materials while reducing their processing costs has led to the development of new non-conventional sintering processes over the last years [1–5]. Currently the most developed non-conventional techniques are the Electric Current Activated/Assisted Sintering (ECAS) [6], and Spark Plasma Sintering (SPS) is likely the most popular of them. SPS allows to sinter, in a short time, a powder compact confined in a die, the whole being heated up by a pulsed DC electric current passage through the die and eventually through the powder itself, the die allowing as well to apply a mechanical pressure in vacuum or inert atmosphere. With SPS it is possible to sinter a wide range of materials like ceramics [7–9], metals [10,11], composites [12–14], or non-equilibrium materials [15,16]. Many advantages over conventional sintering can be attributed to SPS. Among them, rapid heating ramps and mechanical pressure allow for a lowest sintering temperature [17,18]. The SPS sintering of pure α-alumina has been extensively studied [19–25]. It is shown that the densification and the grain size may be adjusted depending on experimental conditions, but the sintering mechanisms are still comparable to conventional free-sintering technique. A significant grain size increase cannot be avoided when the pore pining effect is over (from 95 % of relative density). The modular aspect of SPS technique gives the opportunity to make SPS setups operates both with a mechanical pressure on the sample and the current flow through, or separately [26–31]. In this present work, α-alumina sintering by SPS and pressure-less SPS (PL-SPS) will be compared to α-alumina sintering made by our brand new sintering technique called “pixelated sintering”. The pixelated sintering (PS) is a very original modular sintering technique created and developed by Galtenco Solutions in partnership with the Institut de Recherche sur les Céramiques (Limoges, France) and the Institut de Chimie de la Matiére Condensée de Bordeaux (France). Its name alludes to the heating elements (pixels) placed around the sample and which can be controlled independently of each other. Each pixel is composed by a power supply, a resistive heating element and a thermocouple located as close as possible to the sample. The whole sintering cycle is controlled by a proprietary software that drives each heating element independently, using a thermocouple which is paired to it. The energy delivered to the part is optimized and thermal losses are limited. Beyond energy intensification, sintering is free which opens prospects for the consolidation of complex 3D parts and for transfer to large dimensions. This study aims to show that, using PS, it is possible to sinter α-alumina using natural sintering with a high heating rate and a control of the temperature as good as it is with SPS.

* Corresponding author at: IRCER, UMR CNRS 7315, University of Limoges, 12 rue Atlantis, F-87068 Limoges, France.
E-mail address: inaki.cornu@unilim.fr (I. Cornu).

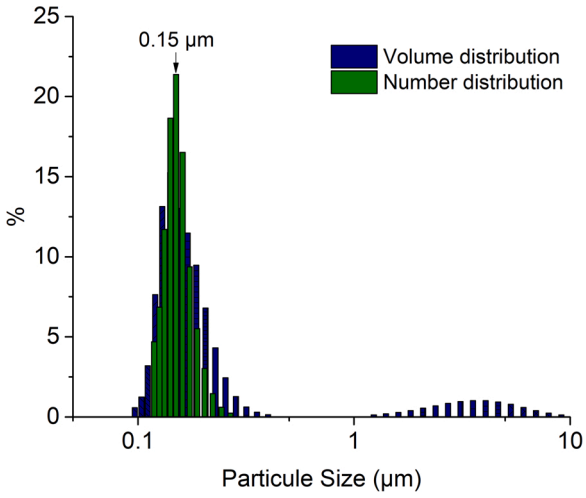

Fig. 1. Particle size distribution of α-alumina.

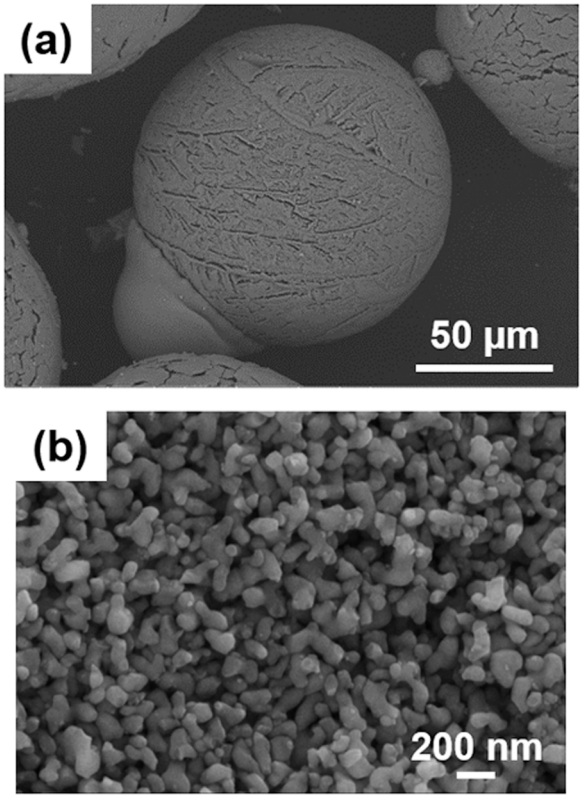

Fig. 2. SEM micrographs (a) spherical granule (b) primary particles.

2. Experimental

2.1. Materials

2.1.1. Alumina powder

All the experiments performed in this study were carried out with a α-alumina powder (purity > 99,9 %,BMA15,Baikowski, France). Fig. 1 shows the volume and number distributions of the BMA15 powder measured by laser granulometry (Mastersizer 2000, Malvern, UK). The volume distribution exhibits a bimodal repartition with a main peak centred around 150 nm and a second peak around 4 μm. This last population corresponds to some aggregates but in small quantity because the number distribution shows only one population centred around 150 nm.

The SEM (VEGA II SBH, TESCAN, Czech Republic) micrograph presented in Fig. 2a indicates that spherical granules with a diameter of about 100 µm form the BMA15 α-alumina powder. These granules contain a large number of primary particles (Fig. 2b) with mean size of 145 nm confirming the granulometry results. The specific surface area was measured by BET as $S_{SSA} = 14\ m^2.g^{-1}$ (Tristar II 3020, Micromeritics, USA), which corresponds to an equivalent spherical particle size of $G_{BET} = 110$ nm.

2.1.2. Preparation of presintered alumina samples

The green BMA15 samples were prepared by a slipcasting method. A slurry was first formulated from a mixture of 70 wt% of BMA15 powder with 0.5 wt% of an electrosteric dispersing agent (Darvan CN) in distilled water. The slurry was firstly homogeneized using a magnetic stirrer for 5 h and secondly placed into a non-contact planetary mixer (ARE-250, THINKY, JAPAN) where the slurry was mixed and degassed at 1000 rmp for 1 min. Then the slurry was casted into a polyoxymethylene cylindric ($\phi = 10$ mm) mould placed itself on a plate of Paris plaster. The green bodies were removed from the mould after 48 h of casting and were dried in air during 24 h at room temperature. The final diameter of all samples was 10 mm and the thickness 3 mm. Finally, a pre-sintering treatment at 1000° C during 1 h under air was performed with a heating ramp of 0.5° $C.min^{-1}$. It led to porous BMA15 ceramics with a relative density measured of 60 % (the theoretical density of BMA15 was taken as 3.94 $g.cm^{-3}$ measured by He pycnometry). The relative density of alumina presintered and sintered samples was determined by Archimedes'method in deionized water.

2.2. Sintering

2.2.1. Presentation of the new pixelated sintering technique

The BMA15 presintered samples were densified using the simple pixelated sintering system presented in Fig. 3. As the considered geometry was a cylinder (10 mm in diameter and 3 mm in thickness), the heating unit was composed by a single pixel made of a graphite diffuser containing one thermocouple which monitored two graphite heating elements placed on the top and bottom of the sample (Fig. 3). The system was assembled on a mica plate (44 × 26 cm) where fixed steel and copper rods were allowing the current flow to Papyex® flexible graphite and so through the two graphite heating elements. The two heating elements were graphite plate (ET10, Graphitech, France) measuring 6 mm long, 4 mm wide and 1 mm thick. They were connected to two low voltage power supplies (30 V, 100 A) wired in parallel, and were dimensioned and machined to obtain a total electric resistance of 0.6 Ω in operation. It was then possible to heat the resistance up to 2000 °C with ramp higher than 200 $°C.min^{-1}$. The temperature was measured by a C thermocouple (W/5%Re-W/26%Re) placed into the graphite diffuser where the sample laid (green point in Fig. 3). Therefore, the measurement of the temperature was done as close as possible to the surface of the sample. In this configuration, the thermocouple controlled the two heat elements at the same time. The upper graphite heat element is placed at 1 cm from the sample and the bottom graphite heat element is placed at 2 cm from the graphite diffuser. Depending on the sintering cycle used and the temperature measured by the thermocouple, the proprietary software (Galtenco Solutions) was able to turn off or on the power supplies connected to the heating elements with a response time of a few milliseconds. The temperature input on the sample surface was then optimized and the risk of thermal gradient minimized. Each component was individually insulated from the heat by alumina insulating whool. This allowed to protect the signal response against electrical interferences but also to avoid a thermal confinement on the sample area, which would have made the temperature measurement biased. The whole set up was finally placed into a vacuum chamber (10^{-1} Pa, Inox 316).

An example of a sintering cycle with maximum temperature of

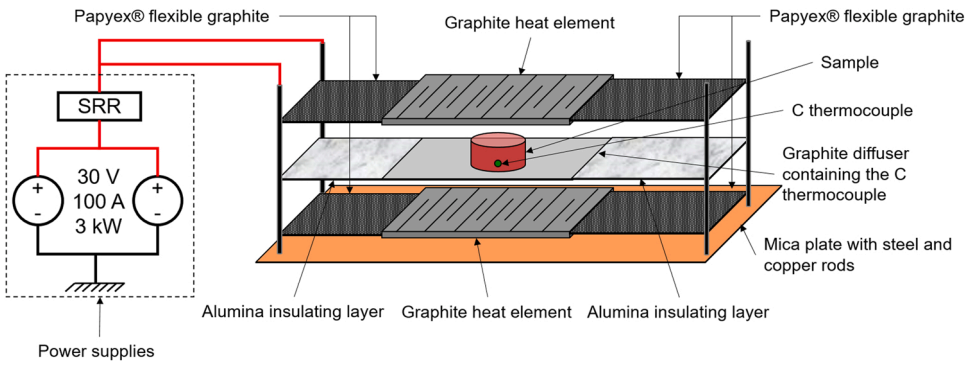

Fig. 3. Pixelated sintering system for densification experiments on BMA15 pre-sintered specimens.

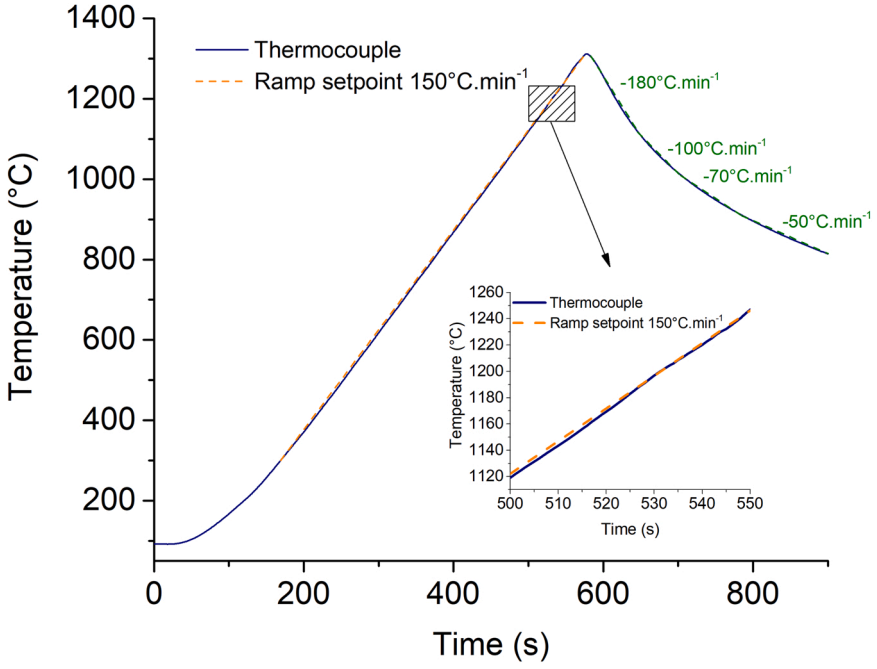

Fig. 4. Example of a pixelated sintering cycle with T_{max} = 1300 °C and heating rate = 150 °C.min^{-1}.

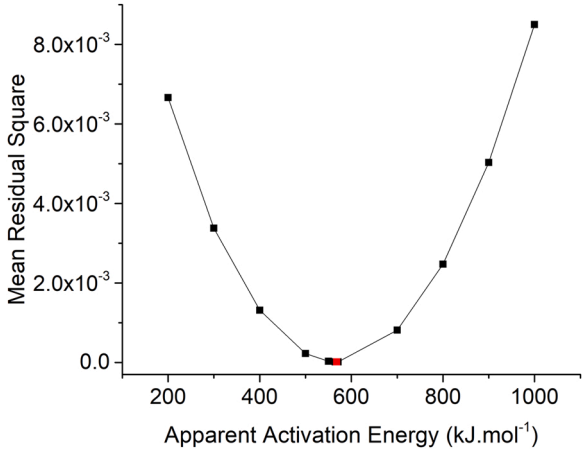

Fig. 5. Mean residual squares for the various values of apparent activation energy. The minimum of the error is obtained at 568 kJ.mol^{-1} (red square).

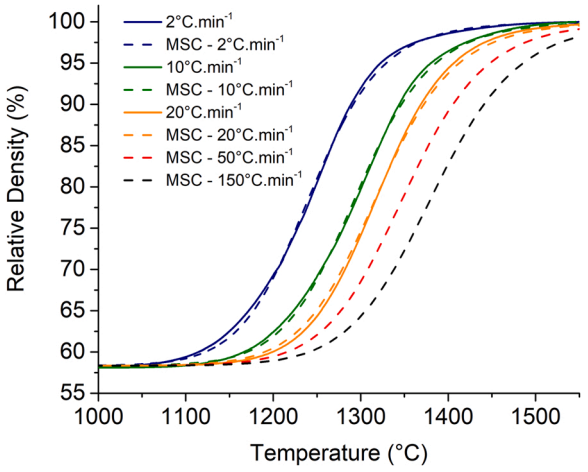

Fig. 6. Comparison of densification curves at 2, 10 and 20 °C.min^{-1} for experiments (blue, green and orange lines) and calculations (blue, green and orange dotted lines). Calculated values at high heating rates: 50 and 150 °C. min^{-1}(red and black dotted lines, respectively) obtained from the MSC model.

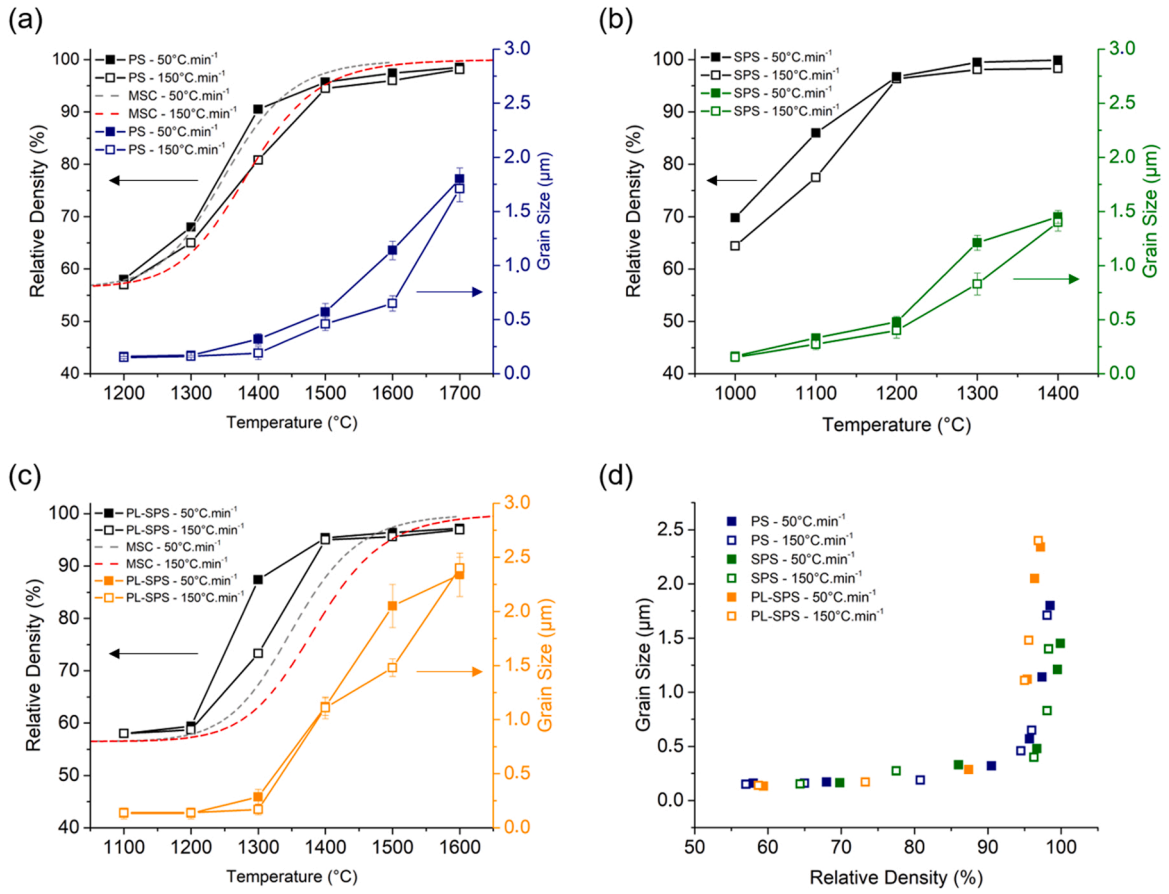

Fig. 7. Relative density and grain size depending on the maximum temperature reached for (a) pixelated sintering, (b) SPS and (c) Pressure-less SPS. (d) Sintering path of α-alumina BMA15 obtained upon all the studied sintering techniques. The heating ramps are represented by closed squares for 50 °C.min^{-1} and empty squares for 150 °C.min^{-1}. In the specific case of high heating rates: 50 and 150 °C.min^{-1} (grey and red dotted lines, respectively) the values were calculated from the MSC model.

1300 °C and a heating rate of 150 °C.min^{-1} is shown in Fig. 4. The C thermocouple placed under the sample maintains or cuts off the power supplies. This is not a continuous heating but rather a pulsed one giving a much better control on the heat input. The cooling is achieved by simply switching off the graphite heating elements (i.e., free cooling). The temperature drops rapidly to 1000 °C (Fig. 4) then, due to the thermal inertia, decreases slowly until reaching 5 °C.min^{-1} below 300 °C. So it is difficult to make a cooling quench with the pixelated sintering technique but the cooling step can be controlled with the same approach as that used for heating ramp. It opens the way to a modular sintering where every steps of the cycle are controlled.

2.2.2. Sintering study

The PS of α-alumina was studied and compared to conventional and SPS sintering. The conventional sintering assessment of our BMA15 powder was made using dilatometry (TMA, Setsys evolution, France). At first, this technique allowed us to extrapolate sintering curves of BMA15 with high heating ramps (50 and 150 °C.min^{-1}). These curves were then compared to the experimental ones obtained by PS. Secondly the PS and SPS performed on BMA15 samples with non-isothermal sintering cycles were compared in terms of densification and grain growth. Two rapid heating ramps were studied: 50 and 150 °C.min^{-1}. The maximum temperature reached depended on the sintering techniques. Grain size of sintered ceramics was determined from SEM micrographs by observation of mirror polished samples and thermally etched at 50 °C below the sintering temperature in air. Grain sizes were measured using the Jeffries' planimetric method [32]. For statistical purposes, the number of measured grains was higher than 500 and 3 different micrographs were taken for each samples. The SPS experiments were carried out on the SPS model Dr.Sinter 825 (Fuji Electronics Industrial Co. Ltd, Japan). For SPS, the BMA15 samples were placed into a cylindrical graphite die (grade 2333, Mersen, France) with a inner diameter of 10 mm. Graphite foils (Papyex® N998, Mersen, France), with a thickness of 0.2 mm, were used to cover the internal surface of the die and the T-shaped punches surfaces. Two configurations were studied. The first was a standard setting where the mechanical pressure applied on the sample was 40 MPa during the whole sintering cycle. The second was called Pressure-Less SPS (PL-SPS). In this setting, the upper graphite T-shaped punch was shortened. The gap between the punch and the sample allowed to avoid a direct contact with the sample and the application of a mechanical pressure on it. This configuration was inspired from Bradbury and Olvesky study [30]. The non-isothermal SPS and PL-SPS tests were performed under vacuum at ($6 < P(Pa) < 14$). The temperature measurements were made using an infrared camera focalized on the external surface of the graphite die containing the sample. A standard pulse sequence (12:2) was chosen for the heating by SPS and PL-SPS.

3. Results and discussion

3.1. Sintering mechanisms

In order to compare the sintering behaviour of our BMA15 powder to other works reported in the literature, a sintering study was firstly undertaken, using dilatometry. The shrinkage curves were recorded as a function of temperature in the 20–1550 °C temperature range for different heating ramps (in static air): 2, 10 and 20 °C.min^{-1}. Analyses of

Table 1
Relative density and grain size obtained for each sintering technique.

Pixelated sintering				
Temperature (°C)	Relative density (%)		Grain size (μm)	
	50 °C.min^{-1}	150 °C.min^{-1}	50 °C.min^{-1}	150 °C.min^{-1}
1200	58	57	0.16 ± 0.01	0.15 ± 0.01
1300	68	65	0.17 ± 0.01	0.16 ± 0.01
1400	90.5	80.8	0.32 ± 0.05	0.19 ± 0.06
1500	95.7	94.5	0.57 ± 0.08	0.46 ± 0.06
1600	97.4	96	1.14 ± 0.08	0.65 ± 0.07
1700	98.5	98.1	1.8 ± 0.1	1.71 ± 0.12
Spark Plasma Sintering				
Temperature (°C)	**Relative density (%)**		**Grain size (μm)**	
	50 °C. min^{-1}	***150 °C. min^{-1}***	***50 °C. min^{-1}***	***150 °C. min^{-1}***
1000	69.8	64.4	0.16 ± 0.04	0.15 ± 0.04
1100	86	77.5	0.33 ± 0.02	0.27 ± 0.05
1200	96.7	96.3	0.48 ± 0.1	0.4 ± 0.1
1300	99.5	98.1	1.21 ± 0.07	0.83 ± 0.1
1400	99.9	98.3	1.45 ± 0.06	1.4 ± 0.08
Pressure-less Spark Plasma Sintering				
Temperature (°C)	**Relative density (%)**		**Grain size (μm)**	
	50 °C. min^{-1}	***150 °C. min^{-1}***	***50 °C. min^{-1}***	***150 °C. min^{-1}***
1200	59.4	57	0.13 ± 0.05	0.14 ± 0.03
1300	87.4	65	0.29 ± 0.07	0.17 ± 0.05
1400	95.4	80.8	1.12 ± 0.08	1.11 ± 0.1
1500	96.4	94.5	2.05 ± 0.2	1.48 ± 0.08
1600	97.2	96	2.34 ± 0.2	2.4 ± 0.1

these data allowed us to determine the Master Sintering Curve (MSC), related to our α-alumina powder. The MSC model, developed by Su and Johnson [33], allows the determination of the sintering activation energy assumed to be a unique value linked to a single densification mechanism. When the model is applicable, the relative density of the material can be predicted from the master sintering curve at any time for any sintering cycle. The MSC model is formulated and based on the densification rate equation combining volume diffusion and grain boundary diffusion mechanisms of the Hansel model [34]. The apparent activation energy, E_a, corresponds to the value where all experimental data, from all heating profiles, converge to a single curve. The convergence is quantified through the minimum of the sum of residual squares for different values of E_a, as shown in Fig. 5 for our α-alumina. From our experimental values, the calculated apparent activation energy is E_a = 568 kJ.mol^{-1}. This obtained value is closed to other values reported in the literature [35,36] for α-alumina. For Bernard-Granger et al. [37], such an E_a can be attributed to a grain boundary diffusion mechanism. Comparison between experimental and calculated sintering behaviours are presented in Fig. 6. The analytic linearization of our MSC is performed by the Blaine et al. equation [38].

Experimental densities of α-alumina samples, heat-treated at 2, 10 and 20 °C.min^{-1} in the 20–1550 °C temperature range are represented by solid blue, green and orange lines respectively. The corresponding blue, green and orange dotted lines represent the calculated curves. The good agreement observed between these curves validates the proposed MSC approach. It can be used to predict the density evolution of BMA15 powder using high heating rates, such as 50 and 150 °C.min^{-1}, as used for our PS, SPS and PL-SPS tests. The density evolution curves are presented, in Fig. 6, in red and black dotted lines for 50 and 150 °C.min^{-1}, respectively.

3.2. Sintering results

Fig. 7 represents the relative density and grain size variations depending on the maximum temperature reached during the different non-isothermal sintering tests performed by PS (Fig. 7a), SPS (Fig. 7b) and PL-SPS (Fig. 7c). Then, the sintering path obtained upon these three techniques is shown in Fig. 7d. Finally all results are also shown in Table 1. For the PS technique (Fig. 7a), seven maximum temperatures were studied: 1100, 1200, 1300, 1400, 1500, 1600 and 1700 °C. The cooling rate was the same as presented earlier in Fig. 4 (i.e., free cooling). A strong increase of relative density is observed between 1300 °C and 1400 °C. At 1400 °C the relative density reached depends on the heating ramp: 90.5 % for 50 °C.min^{-1} and 80.8 % for 150 °C.min^{-1}. Then the relative densities reach around 95 % at 1500 °C. The SEM micrographs in Fig. 8 (blue frame) illustrate the transition from open porosities to closed porosities for the PS technique. We observe a densification delay between the two studied heating ramps (Fig. 7a). This delay can be assigned to a kinetic effect due to a different holding time at high temperature (i.e. in between 1400 and 1500 °C). Finally the relative densities progress together reaching about 98 % at 1700 °C. Calculated values of densities for 50 and 150 °C.min^{-1} (grey and red dotted lines, respectively) obtained from the MSC model are also plotted. We observe for the two heating ramps that the sintering initiation starts in the same temperature range, towards 1300 °C. The experimental sigmoid curves inflexion point, where the densification rate is the highest, is superimposed on corresponding MSC curves. The experimental and calculated curves separate with each other for relative densities around 92 % for 50 °C.min^{-1} and around 95 % for 150 °C.min^{-1}. The pixelated sintering follows the MSC predicting behaviour. Thus, it can be considered as a conventional sintering technique. The grain size variation (blue curves in Fig. 7a) shows a constant grain growth from 1200 to 1500 °C. At 1400 °C, the gap between the grain size observed for the two heating ramps is linked to the gap of relative densities. The difference of holding time at high temperature is brought to light at 1600 °C. Indeed for the 50 °C.min^{-1} heating rate, the pore pinning effect [39,40] is already over. Therefore, we observe a significant increase of the grain size. For the 150 °C.min^{-1} heating rate, the end of pore-pinning effect takes place between 1600 and 1700 °C. Hence, at 1700 °C, the grain sizes for the two heating ramps are similar. For the SPS standard technique (Fig. 7b), five maximum temperatures were studied: 1000, 1100, 1200, 1300 and 1400 °C. The cooling rate of 25 °C.min^{-1} was controlled this time to avoid thermal shock and cracks in sintered BMA15 samples. From 1000 °C, a slight increase of relative density is observed for the both ramps. This low enhancement could come from a particles rearrangement due to the application of the mechanical pressure (40 MPa) on the BMA15 samples throughout the sintering cycle. At 1100 °C, a clear relative density difference is observed between both heating rates.

Indeed 86 % and 77.5 % relative densities of SPS samples are obtained for 50 and 150 °C.min^{-1} respectively. Thus, the sintering initiation is already started at this temperature. Once more, a different temperature holding time could explain this discrepancy. At 1200 °C, the relative densities are around 96 %. The transition from open porosities to closed porosities for the SPS technique is occurring between 1100 °C and 1200 °C. As well as pixelated sintering, this transition is illustrated by SEM micrographs in Fig. 8 (green frame). The rapid densification observed for 150 °C.min^{-1} (77.5–96.3 % from 1300 to 1400 °C) is also shown in Santanach et al. study [24]. Finally, relative densities close to 99 % are obtained for the both heating ramps at higher temperatures (1300 and 1400 °C). The grain size variation (green curves in Fig. 7b) is the same as pixelated sintering. At 1300 °C, we have, once more, a difference between the both heating ramps due to the end of pore-pining effect. Finally at 1400 °C, the grain sizes heating rates for both join each other and are similar. We can notice the interest of SPS sintering to obtain dense materials with a temperature 200° C lower than PS and without isothermal holding. However, even if the contribution of mechanical application is clear, it does not allow to avoid, in this SPS conditions, the significant grain growth phenomenon when the sample relative density reaches 95 %.

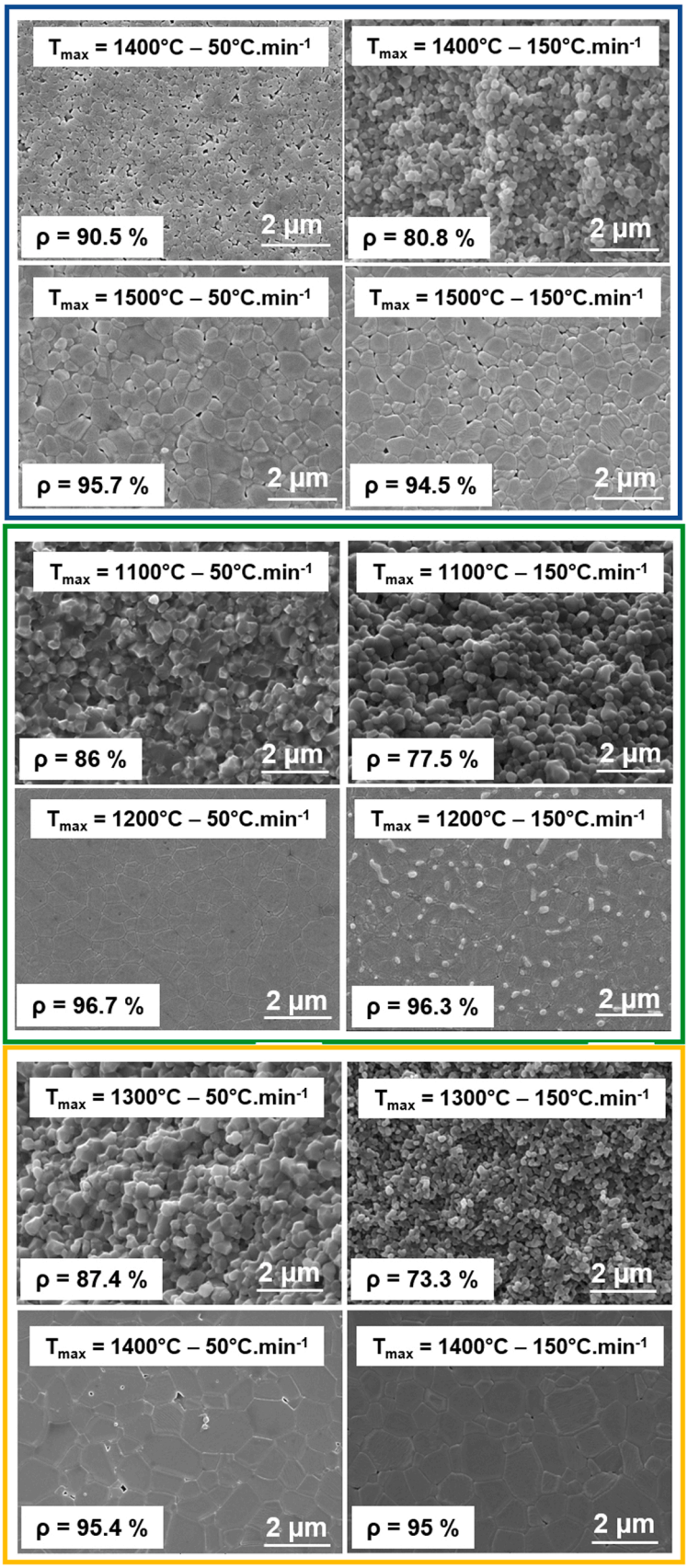

Fig. 8. SEM micrographs show α-alumina microstructures sintered through different temperatures (T_{max}) and heat ramps (50 and 150 °C.min^{-1}) by (blue frame) pixelated sintering, (green frame) SPS and (orange frame) pressure-less SPS. ρ corresponds to the sample relative density.

For the PL-SPS technique (Fig. 7c), six maximum temperatures were studied: 1100, 1200, 1300, 1400, 1500 and 1600 °C. The cooling rate was controlled at 100 °C.min^{-1}. From 1100–1200 °C the relative densities slightly increase. This is at 1300 °C that we observe a significant difference between both heating ramps. Indeed, for the 50° C.min^{-1} ramp, the densification is already at an advanced stage with a relative density of 87.4 %. For the 150 °C.min^{-1} ramp, the relative density is only 73.3 %. The experimental sintering curves join each other at 1400 °C with a relative density around 95 %. The SEM micrographs in Fig. 8 (orange frame) illustrate the pore-closing transition for the PL-SPS technique. Finally relative densities slowly evolve up to 97 % from 1500 to 1600 °C. The PL-SPS is a technique where the configuration is studied to avoid direct mechanical contact with sample and thus the application of a mechanical pressure on it. We note a shift between experimental and calculated values at high heating rates (grey and red dotted lines for 50 et 150 °C.min^{-1} respectively) obtained from the MSC model. If we add 75 °C to each point of the experimental curves, it seems to follow back the MSC curves behaviour until relative density reaches around 90 ~ 92 %. This temperature difference could be explained by the temperature measurement method used for the SPS and PL-SPS setups, namely an infrared optical camera. The temperature measured is the temperature of the graphite die external surface and not the real temperature of the sample that is here probably higher. This observation is already reported in the literature [41–46]. It is shown that the inside and outside temperature difference is exacerbated in the case of the sintering of insulated materials. Moreover a FEM analysis of SPS sintering of alpha alumina has been carried out by Wang et al. [47] considering a large range of die sizes, heating rates and uniaxial stresses. It shows that, for a SPS die with inner diameter of 12 mm, radial and axial thermal gradients occur. In our study, these gradients are notably exacerbated in our PL-SPS setup due to the air film presence between the non-touching upper graphite punch and the sample. That is why such a gap around 75 °C is observed between experimental and calculated curves. A further study of our PL-SPS must be made if we want to optimize PL-SPS. A higher grain size for PL-SPS in comparison with PS and SPS should be noted. Once more, the error in the internal temperature measurement could be the origin. Finally a comparison between the different sintering paths obtained from the three sintering techniques is reported in Fig. 7d. The graph shows the grain size obtained depending on the relative density. It confirms that the sintering behaviour is the same between SPS, PL-SPS and PS. In the same sintering conditions, PS allows to access to the same results as the sintering of α-alumina by SPS in terms of densification and grain growth behaviour with high heating ramps. Thus PS can be classified among so-called fast sintering techniques.

4. Conclusion

This study aimed to show the ability of PS sintering technique to obtain results close to those obtained with other well-known fast sintering techniques: SPS and PL-SPS. Here we used a high purity submicron size α-alumina to compare SPS, PL-SPS and PS in terms of densification and grain growth. We showed as expected that SPS has its own densification behaviour because of the application of pressure. We succeeded anyway to get densification and grain size with PS comparable to SPS and PL-SPS. Furthermore, we demonstrated the same sintering behaviour between the three techniques. The process undertaken with our novel PS technique is not really to compete with SPS or other fast sintering techniques but rather to offer an alternative sintering technique with many advantages: free and fast sintering into controlled-atmospheres (under air, vacuum or inert gas) with a fine and localised heat input for energy intensification. This totally modular technique can also represent a new way in modular sintering like multi-step sintering, or else the large size materials and complex architecture sintering. This last very important point for industrial leveraging of PS will be described in a future article.

Funding

This work was supported by an institutional grant of the French National Research Agency (ANR-17-CE08-0033 PIXUFAST project).

Declaration of Competing Interest

The authors declare that they have no known competing financial interests or personal relationships that could have appeared to influence the work reported in this paper.

Acknowledgements

The authors want to acknowledge Mrs. Marion Vandenhende for her technical support in carrying out the SPS experiments.

References

[1] G. Degroat, One-shot powder metal parts, Am. Mach. 109 (11) (1965) 107–109.
[2] M. Cologna, B. Rashkova, R. Raj, Flash sintering of nanograin zirconia in < 5 s at 850 °C, J. Am. Ceram. Soc. 93 (11) (2010) 3556–3559.
[3] W.H. Sutton, Microwave processing of ceramics - an overview, MRS Proc. 269 (1992), https://doi.org/10.1557/PROC-269-3.
[4] R. E. Riman, V. Atakan, Method of hydrothermal liquid phase sintering of ceramic materials and products derived therefrom, US patent 8, 313, 802. 2010.
[5] C.A. Randall, J. Guo, A. Baker, M. Lanagan, G. Hanzheng, Cold sintering ceramics and composites, Google Patents, 2017.
[6] S. Grasso, Y. Sakka, G. Maizza, Electric current activated/assis- ted sintering (ECAS): a review of patents 1906-2008, Sci. Technol. Adv. Mater. 10 (5) (2009), 053001.
[7] Z.-H. Zhang, F.-C. Wang, J. Luo, S.-K. Lee, L. Wang, Processing and characterization of fine-grained monolithic SiC ceramic synthesized by spark plasma sintering, Mater. Sci. Eng. A 527 (7–8) (2010) 2099–2103.
[8] A. Bellosi, F. Monteverde, D. Sciti, Fast densification of ultra-high-temperature ceramics by spark plasma sintering, Int. J. Appl. Ceram. Technol. 3 (1) (2006) 32–40, https://doi.org/10.1111/j.1744-7402.2006.02060.x.
[9] U. Anselmi-Tamburini, J. Garay, Z. Munir, A. Tacca, F. Maglia, G. Spinolo, Spark plasma sintering and characterization of bulk nanostructured fully stabilized zirconia: part I. Densification studies, J. Mater. Res. 19 (11) (2004) 3255–3262, https://doi.org/10.1557/JMR.2004.0423.
[10] H. Kwon, D.H. Park, Y. Park, J.F. Silvain, A. Kawasaki, Y. Park, Spark plasma sintering behavior of pure aluminum depending on various sintering temperatures, Met. Mater. Int. 16 (1) (2010) 71–75, https://doi.org/10.1007/s12540-010-0071-2.
[11] Z. Zhang, F. Wang, S. Lee, Y. Liu, J. Cheng, Y. Liang, Microstructure characteristic, mechanical properties and sintering mechanism of nanocrystalline copper obtained by SPS process, Mater. Sci. Eng. A 523 (1–2) (2009) 134–138, https://doi.org/10.1016/j.msea.2009.07.016.
[12] B. Basu, J.-H. Lee, D.-Y. Kim, Development of WC-ZrO_2 nano- composites by spark plasma sintering, J. Am. Ceram. Soc. 87 (2) (2004) 317–319, https://doi.org/10.1111/j.1551-2916.2004.00317.x.
[13] N. Ghosh, S. Harimkar, Consolidation and synthesis of MAX phases by spark plasma sintering (SPS): a review, in: Advances in Science and Technology of Mn.1AXn Phases, Elsevier, 2012, pp. 47–80, https://doi.org/10.1533/9780857096012.47.
[14] T. Hérisson de Beauvoir, K. Tsuji, X. Zhao, J. Guo, C. Randall, Cold sintering of ZnO-PTFE: utilizing polymer phase to promote ceramic anisotropic grain growth, Acta Mater. 186 (2020) 511–516, https://doi.org/10.1016/j.actamat.2020.01.002.
[15] J. Suffner, M. Lattemann, H. Hahn, L. Giebeler, C. Hess, I.G. Cano, S. Dosta, J. M. Guilemany, C. Musa, A.M. Locci, R. Licheri, R. Orrú, G. Cao, Microstructure evolution during spark plasma sintering of meta- stable (ZrO_2 -3 mol% Y_2O_3)-20 wt% Al_2O_3 composite powders, J. Am. Ceram. Soc. 93 (9) (2010) 2864–2870, https://doi.org/10.1111/j.1551-2916.2010.03752.x.
[16] T. Herisson de Beauvoir, A. Sangregorio, I. Cornu, M. Josse, Synthesis, sintering by Cool-SPS and characterization of $A_2Cu(CO_3)_2$ (A = K, Na): evidences for multiferroic and magnetoelectric cupricarbonates, Dalton Trans. 49 (23) (2020) 7820–7828, https://doi.org/10.1039/D0DT00814A.
[17] K. Rajeswari, U. Hareesh, R. Subasri, D. Chakravarty, R. Johnson, Comparative evaluation of spark plasma (SPS), microwave (MWS), two stage sintering (TSS) and conventional sintering (CRH) on the densification and micro structural evolution of fully stabilized zirconia ceramics, Sci. Sinter. 42 (3) (2010) 259–267, https://doi. org/10.2298/SOS1003259R.
[18] T. Herisson de Beauvoir, A. Sangregorio, I. Cornu, C. Elissalde, M. Josse, Cool-SPS: an opportunity for low temperature sintering of thermodynamically fragile materials, J. Mater. Chem. C 6 (9) (2018) 2229–2233, https://doi.org/10.1039/C7TC05640K.
[19] Y. Makino, M. Sakaguchi, J. Terada, K. Akamatsu, Consolidation of ultrafine alumina powders with SPS method, J. Jpn. Soc. Powder Powder Metall. 54 (4) (2007) 219–225, https://doi.org/10.2497/jjspm.54.219.

[20] M. Demuynck, J.-P. Erauw, O. Van der Biest, F. Delannay, F. Cambier, Densification of alumina by SPS and HP: a comparative study, J. Eur. Ceram. Soc. 32 (9) (2012) 1957–1964, https://doi.org/10.1016/j.jeurceramsoc.2011.10.031.

[21] P. Guyot, G. Antou, N. Pradeilles, A. Weibel, M. Vandenhende, G. Chevallier, A. Peigney, C. Estournès, A. Maiˆtre, Hot pressing and spark plasma sintering of alumina: discussion about an analytical modelling used for sintering mechanism determination, Scr. Mater. 84–85 (2014) 35–38, https://doi.org/10.1016/j.scriptamat.2014.04.013.

[22] Y. Aman, V. Garnier, E. Djurado, Spark plasma sintering kinetics of pure α -alumina, J. Am. Ceram. Soc. 94 (9) (2011) 2825–2833, https://doi.org/10.1111/j.1551-2916.2011.04424.x.

[23] Z. Shen, M. Johnsson, Z. Zhao, M. Nygren, Spark plasma sintering of alumina, J. Am. Ceram. Soc. 85 (8) (2002) 1921–1927, https://doi.org/10.1111/j.1151-2916.2002.tb00381.x.

[24] J.G. Santanach, A. Weibel, C. Estournès, Q. Yang, C. Laurent, A. Peigney, Spark plasma sintering of alumina: study of parameters, formal sintering analysis and hypotheses on the mechanism(s) involved in densification and grain growth, Acta Mater. 59 (4) (2011) 1400–1408, https://doi.org/10.1016/j.actamat.2010.11.002.

[25] C. Manière, L. Durand, A. Weibel, C. Estournès, Spark-plasma-sintering and finite element method: from the identification of the sintering parameters of a submicronic α -alumina powder to the development of complex shapes, Acta Mater. 102 (2016) 169–175, https://doi.org/10.1016/j.actamat.2015.09.003.

[26] D. Giuntini, X. Wei, A.L. Maximenko, L. Wei, A.M. Ilyina, E.A. Olevsky, Initial stage of free pressureless spark-plasma sintering of vanadium carbide: determination of surface diffusion parameters, Int. J. Refract. Met. Hard Mater. 41 (2013) 501–506, https://doi.org/10.1016/j.ijrmhm.2013.06.009.

[27] Y.-S. Lin, M.A. Meyers, E.A. Olevsky, Microchannelled hydroxyapatite components by sequential freeze drying and free pressureless spark plasma sintering, Adv. Appl. Ceram. 111 (5–6) (2012) 269–274, https://doi.org/10.1179/1743676111Y.0000000067.

[28] Y. Aman, V. Garnier, E. Djurado, Pressure-less spark plasma sintering effect on non-conventional necking process during the initial stage of sintering of copper and alumina, J. Mater. Sci. 47 (15) (2012) 5766–5773, https://doi.org/10.1007/s10853-012-6469-0.

[29] L. Bertolla, I. Dlouhý, P. Tatarko, A. Viani, A. Mahajan, Z. Chlup, M.J. Reece, A. R. Boccaccini, Pressureless spark plasma-sintered Bioglass® 45S5 with enhanced mechanical properties and stress-induced new phase formation, J. Eur. Ceram. Soc. 37 (7) (2017) 2727–2736, https://doi.org/10.1016/j.jeurceramsoc.2017.02.003.

[30] W.L. Bradbury, E.A. Olevsky, Production of SiC-C composites by free-pressureless spark plasma sintering (FPSPS), Scr. Mater. 63 (1) (2010) 77–80, https://doi.org/10.1016/j.scriptamat.2010.03.009.

[31] Y. Quan, F. Zhang, H. Rebl, B. Nebe, O. Keßler, E. Burkel, Ti6Al4V foams fabricated by spark plasma sintering with post-heat treatment, Mater. Sci. Eng. A 565 (2013) 118–125, https://doi.org/10.1016/j.msea.2012.12.026.

[32] R. Allen, Standard Test Methods for Determining Average Grain Size (F112), Annual Book of ASTM Standards, Metal-Mechanical Testing; Elevated and Low Temperature Tests, ASTM, 1999.

[33] H. Su, D.L. Johnson, Master sintering curve: a practical approach to sintering, J. Am. Ceram. Soc. 79 (12) (1996) 3211–3217, https://doi.org/10.1111/j.1151-2916.1996.tb08097.x.

[34] J.D. Hansen, R.P. Rusin, M.-H. Teng, D.L. Johnson, Combined-stage sintering model, J. Am. Ceram. Soc. 75 (5) (1992) 1129–1135, https://doi.org/10.1111/j.1151-2916.1992.tb05549.x.

[35] J. Tatami, Y. Suzuki, T. Wakihara, T. Meguro, K. Komeya, Control of shrinkage during sintering of alumina ceramics based on master sintering curve theory, Key Eng. Mater. 317-318 (2006) 11–14, https://doi.org/10.4028/www.scientific.net/KEM.317-318.11.

[36] F. Zuo, S. Saunier, S. Marinel, P. Chanin-Lambert, N. Peillon, D. Goeuriot, Investigation of the mechanism(s) controlling microwave sintering of α -alumina: influence of the powder parameters on the grain growth, thermodynamics and densification kinetics, J. Eur. Ceram. Soc. 35 (3) (2015) 959–970, https://doi.org/ 10.1016/j.jeurceramsoc.2014.10.025.

[37] G. Bernard-Granger, C. Guizard, A. Addad, Sintering of an ultra pure α -alumina powder: I. Densification, grain growth and sintering path, J. Mater. Sci. 42 (15) (2007) 6316–6324, https://doi.org/10.1007/s10853-006-1206-1.

[38] D.C. Blaine, S.-J. Park, R.M. German, Linearization of master sintering curve, J. Am. Ceram. Soc. 92 (7) (2009) 1403–1409, https://doi.org/10.1111/j.1551-2916.2009.03011.x.

[39] R.M. German, Sintering Theory and Practice, Wiley,, New York, 1996.

[40] A.S.A. Chinelatto, E.M. de Jesus Agnolon Pallone, A.M. de Souza, M.K. Manosso, A. L. Chinelatto, R. Tomasi, Mechanisms of microstructure control in conventional sintering, in: A. Lakshmanan (Ed.), Sintering of Ceramics, IntechOpen, Rijeka, 2012, https://doi.org/10.5772/33616.

[41] D. Chakravarty, A.H. Chokshi, Direct characterizing of densification mechanisms during spark plasma sintering, J. Am. Ceram. Soc. 97 (3) (2014) 765–771, https:// doi.org/10.1111/jace.12796.

[42] U. Anselmi-Tamburini, S. Gennari, J. Garay, Z. Munir, Fundamental investigations on the spark plasma sintering/synthesis process, Mater. Sci. Eng. A 394 (1–2) (2005) 139–148, https://doi.org/10.1016/j.msea.2004.11.019.

[43] S.-X. Song, Z. Wang, G.-P. Shi, Heating mechanism of spark plasma sintering, Ceram. Int. 39 (2) (2013) 1393–1396, https://doi.org/10.1016/j.ceramint.2012.07.080.

[44] D. Tiwari, B. Basu, K. Biswas, Simulation of thermal and electric field evolution during spark plasma sintering, Ceram. Int. 35 (2) (2009) 699–708, https://doi.org/ 10.1016/j.ceramint.2008.02.013.

[45] S. Muñoz, U. Anselmi-Tamburini, Temperature and stress fields evolution during spark plasma sintering processes, J. Mater. Sci. 45 (23) (2010) 6528–6539, https:// doi.org/10.1007/s10853-010-4742-7.

[46] J. Räthel, M. Herrmann, W. Beckert, Temperature distribution for electrically conductive and non-conductive materials during field assisted sintering (FAST), J. Eur. Ceram. Soc. 29 (8) (2009) 1419–1425, https://doi.org/10.1016/j.jeurceramsoc.2008.09.015.

[47] C. Wang, L. Cheng, Z. Zhao, FEM analysis of the temperature and stress distribution in spark plasma sintering: Modelling and experimental validation, Computational Materials Science 49 (2) (2010) 351–362, https://doi.org/10.1016/j.commatsci.2010.05.021.